Transactions of Tianjin University (2023) 29:89–100
https://doi.org/10.1007/s12209-022-00338-7

RESEARCH ARTICLE

Ultrasmall NiS_2 Nanocrystals Embedded in Ordered Macroporous Graphenic Carbon Matrix for Efficiently Pseudocapacitive Sodium Storage

Zhaozhao Liu[1] · Jiang Wang[1] · Ran Bi[2] · Pinyi Zhao[3,4] · Mengqian Wu[1] · Xinyu Liu[1] · Likun Yin[2] · Chengyang Wang[1] · Mingming Chen[1] · Kemeng Ji[1,5]

Received: 14 June 2022 / Revised: 30 June 2022 / Accepted: 22 July 2022 / Published online: 24 August 2022
© The Author(s) 2022

Abstract

Sodium-ion hybrid capacitor (SIHC) is one of the most promising alternatives for large-scale energy storage due to its high energy and power densities, natural abundance, and low cost. However, overcoming the imbalance between slow Na^+ reaction kinetics of battery-type anodes and rapid ion adsorption/desorption of capacitive cathodes is a significant challenge. Here, we propose the high-rate-performance NiS_2@OMGC anode material composed of monodispersed NiS_2 nanocrystals (8.8 ± 1.7 nm in size) and N, S-co-doped graphenic carbon (GC). The NiS_2@OMGC material has a three-dimensionally ordered macroporous (3DOM) morphology, and numerous NiS_2 nanocrystals are uniformly embedded in GC, forming a core–shell structure in the local area. Ultrafine NiS_2 nanocrystals and their nano–microstructure demonstrate high pseudocapacitive Na-storage capability and thus excellent rate performance (355.7 mAh/g at 20.0 A/g). A SIHC device fabricated using NiS_2@OMGC and commercial activated carbon (AC) cathode exhibits ultrahigh energy densities (197.4 Wh/kg at 398.8 W/kg) and power densities (43.9 kW/kg at 41.3 Wh/kg), together with a long life span. This outcome exemplifies the rational architecture and composition design of this type of anode material. This strategy can be extended to the design and synthesis of a wide range of high-performance electrode materials for energy storage applications.

Keywords Sodium-ion battery · Sodium-ion hybrid capacitor · Three-dimensionally ordered macroporous structure · Graphenic carbon · NiS_2 nanocrystals

Introduction

Sodium-ion hybrid capacitors (SIHCs) have emerged as an essential alternative for electrochemical energy storage in modern society due to their natural abundance, environmental friendliness, and low cost of sodium resources [1, 2]. Generally, a SIHC consists of a battery-type anode with high specific capacity and a supercapacitor-type cathode with high-rate capability, resulting in a promising candidate to achieve considerable energy and power densities simultaneously [3–5]. However, the kinetics between the rapid ion adsorption/desorption in capacitive cathodes and the sodiation/desodiation in battery-type anodes are mismatched during the charging/discharging process. In this regard, the major challenge for high-performance SIHCs lies in exploring desirable sodium-ion storage anode materials to overcome the kinetics imbalance [6].

To date, miscellaneous anode candidates of sodium-ion batteries (SIBs) have been attempted as anode materials for

✉ Kemeng Ji
kmji@tju.edu.cn

[1] Key Laboratory for Green Chemical Technology of Ministry of Education, School of Chemical Engineering and Technology, Tianjin University, Tianjin 300350, China

[2] Comprehensive Energy Research Center, Science and Technology Research Institute, China Three Gorges Corporation, Beijing 100038, China

[3] Institute for Materials Discovery, University College London, London WC1E 7JE, UK

[4] Department of Chemistry, University College London, London WC1H 0AJ, UK

[5] Department of Materials Science, Graduate School of Engineering, Tohoku University, Sendai 980-8579, Japan

SIHCs [3]. There are three sodium storage mechanisms: intercalation, conversion, and alloying [7, 8]. Intercalation mechanisms refer to the insertion of sodium ions into lattice materials that exhibit small volume change and thus maintain structural integrity, such as carbon-based materials. Conversion and alloying mechanisms refer to reacting with sodium via multi-electron conversion and forming intermetallic binary compounds by alloying with sodium. The materials of these two mechanisms typically exhibit poor conductivity and undergo significant volume expansion and contraction during charging and discharging, which causes material pulverization and electrode fragmentation, resulting in reduced capacity and poor rate performance [9]. Among conversion-type anode materials, transition metal sulfides, particularly nickel-based sulfides, have attracted tremendous attention due to abundant resources, low price, and high theoretical specific capacity (ca. 446, 591, and 879 mAh/g for Ni_3S_2, NiS, and NiS_2, respectively) [10]. In various nickel-based sulfides, nickel disulfide (NiS_2) possesses the highest theoretical specific capacity but suffers from the worst electrical conductivity and the largest volume change [11, 12]. Furthermore, metal sulfide anodes in SIBs easily fail due to the generation and dissolution of polysulfides during cycling [13]. Regardless, NiS_2 has been shown to possess strong adsorption of polysulfides and high conversion of soluble polysulfides into insoluble Na_2S_2/Na_2S [14].

Several useful strategies have been employed to alleviate the awful electrical conductivity and volume change of NiS_2 anode materials. A common route is to combine a highly stable and conductive carbon-based matrix (e.g., carbon nanotubes [15], carbon nanofibers [16], and reduced graphene oxide [17]), which can improve electrical conductivity and structural stability to a certain degree. For example, Li et al. [18] fabricated a graphene network-supported NiS_2 nanocrystal, whose reversible capacity reached 580.6 mAh/g at 5.0 A/g. However, the high cost of graphene makes it difficult to be used on a large scale. Furthermore, electrochemical performance, particularly high-rate capability, which is typically limited by sluggish Na^+ solid diffusion [19], needs to be improved. Tremendous efforts have been made in nanoengineering and structure design to accelerate the sluggish Na^+ diffusion kinetics. Nanoscale materials greatly diminish the effects of volume change and shorten diffusion paths. Besides, the three-dimensionally ordered macroporous (3DOM) framework has great potential to enhance the rate performance. With the intrinsic hierarchical pores, highly developed channels, and bicontinuous pore structure, the 3DOM architecture has the expected functions of accommodating volume expansion, promoting ion transport, and ensuring electron conduction [19].

Motivated by the above, we developed a 3DOM-structured NiS_2@OMGC composite through a simple thiourea (CH_4N_2S) pyrolysis-assisted colloidal crystal template method. Numerous NiS_2 nanocrystals (~ 8.8 ± 1.7 nm in diameter) are uniformly embedded in the nano-onion GC units of the 3DOM matrix, yielding a core–shell structure locally. This nano–microstructure can not only alleviate the volume change but also will realize high nanocrystallization (< 10 nm in size) and monodisperse distribution of NiS_2, which is beneficial to improving their rate performances. This conversion-type NiS_2 anode delivers almost 100% pseudocapacitive Na-storage behavior and excellently high-rate performance (355.6 mAh/g at 20.0 A/g), together with remarkable cycling stability due to the synergistic effect between the ultrafine NiS_2 particles and 3DOM GC matrix (68.5 and 31.5 wt%, respectively). The simultaneously high energy and power densities of an as-configured NiS_2@OMGC//AC SIHC device, coupled with the NiS_2@OMGC anode and the commercially available activated carbon (AC) cathode, can further confirm the rationality of the NiS_2@OMGC anode in its architecture and composition. Such a design strategy could be effective for many other battery-type electrode materials beyond sodium-based systems.

Experimental Section

Chemicals and Reagents

Methyl methacrylate (MMA, 98%) was purchased from Shanghai Macklin Biochemical Co., Ltd. Potassium persulfate ($K_2S_2O_8$, AR grade), nickel nitrate hexahydrate ($Ni(NO_3)_2{\cdot}6H_2O$, 98%), thiourea (CH_4N_2S, 99%), and citric acid ($C_6H_8O_7$, AR grade) were procured from Shanghai Aladdin Biochemical Technology Co., Ltd. All reagents were used as received without further purification.

Materials Synthesis

The polymethyl methacrylate (PMMA) microsphere template was synthesized by the reported method [20]. In a typical procedure, nickel nitrate hexahydrate and citric acid were mixed and dissolved in deionized water with molar concentrations of 2.0 mol/L and 1.0 mol/L, respectively. The structurally ordered template of PMMA microspheres was impregnated in the above solution after vigorous stirring for 1 h until the precursor solution filled its interstitial spaces. The excess precursor solution was then removed by filtration. After drying, the nickel salt-impregnated PMMA template precursors were carbonized for 30 min under a nitrogen atmosphere at 500 °C with a ramp rate of 2 °C/min. After cooling the furnace to room temperature, the product denoted as Ni@OMGC was prepared.

The as-prepared Ni@OMGC underwent a thiourea-treatment process with a mass ratio of 1:5 in a nitrogen atmosphere at 350 °C for 3 h with a ramp rate of 5 °C/min. Ni@OMGC

and thiourea were placed downstream and upstream of the tube furnace. The NiS_2@OMGC product was obtained after the furnace was cooled to room temperature.

Material Characterization

The morphology of the products was characterized using a field-emission scanning electron microscope (SEM, S-4800) and a transmission electron microscope (TEM, JEM-F200) equipped with energy-dispersive spectroscopy (EDS). A Bruker D8 Advance X-ray diffractometer (XRD) was used to scan the product from 10 to 90° with Cu Kα radiation. Raman spectra were obtained using a DXR Microscope spectrometer equipped with a 532 nm laser. The N_2 adsorption/desorption isotherm was measured at 77 K using a BSD-PS(M) volumetric adsorption analyzer for measuring specific surface area and porosity distribution. The pore size distribution (PSD) was calculated using a non-local density functional theory model from the adsorption isotherm. X-ray photoelectron spectroscopy (XPS, ESCALAB Xi+) was examined using monochromatic Al-Kα radiation (1486.6 eV), and the binding energy was calibrated with a correction value of 284.8 eV for C 1*s*.

Electrochemical Measurements

The working electrodes were prepared by casting a slurry of the as-prepared product (80 wt%), super P (10 wt%), and poly-(vinylidene fluoride) (PVDF, 10 wt%) dispersed in N-methyl-2-pyrrolidone (NMP) onto a copper foil with a doctor blade, followed by drying at 80 °C overnight. The obtained electrodes were cut into circular disks with a diameter of 13.0 mm. The mass loading of NiS_2@OMGC was 0.8–1.0 mg/cm^2. The Na^+ half-cells were assembled in an Ar-filled glovebox using Na foils as the counter and reference electrodes and GF/D glass fibers as the separators. The electrolyte was $NaPF_6$ of 0.8 mol/L in diglyme (DEGDME).

For the SIHC device, the cathode was prepared by mixing the AC (YP-50, 80 wt%), super P (10 wt%), PVDF (10 wt%) binder in NMP and then coated on an Al foil. For the anode, the NiS_2@OMGC electrodes in the Na^+ half-cells were cycled at 0.1 A/g for five cycles before being discharged to 0.01 V and then disassembled from the cells in the glove box. In a SIHC full cell, the active mass ratio of the cathode to the anode was 3:1. The electrolyte was the same 0.8 mol/L $NaPF_6$ in DEGDME. Based on the total mass/volume of anode and cathode active materials, the energy densities (*E*, Wh/kg) and power densities (*P*, W/kg) of the SIHCs were calculated as follows:

$$C = (I \times \Delta t) / (m \times \Delta V) \tag{1}$$

$$\Delta V = V_{\max} - V_{\min} \tag{2}$$

$$E = \int_{t_1}^{t_2} IVdt \tag{3}$$

$$P = \frac{E}{t} \tag{4}$$

where I is the constant current; Δt is the discharge time; m is the total active mass/volume of anode and cathode; t_1 and t_2 are the start time and end time in the discharge process, respectively; $V_{\max}$ is the potential at the beginning of discharge after the IR drop; and $V_{\min}$ is the terminal voltage in the discharge process.

Kinetic Analyses Methods

Electrochemical impendence spectroscopy (EIS) measurements were performed in situ on an Iviumstat electrochemical workstation in impedance potential scan mode. The implementation was an analog to the impedance constant E (a range of frequencies is applied at a constant DC potential) variant. Meanwhile, it was repeated at the range of 3.0–0.01 V and 0.01–3.0 V, respectively.

The diffusion coefficient of Na^+ ion (D_{Na+}) could be calculated with the following equations [21]:

$$D_{Na^+} = \frac{R^2T^2}{2A^2n^4F^4C^2\sigma^2} \tag{5}$$

$$Z' = R_s + R_{ct} + \sigma\omega^{-1/2} \tag{6}$$

where R is the gas constant; T is the absolute temperature; A is the surface area of the anode; n is the number of electrons per molecule during the reaction; F is the faraday constant; C is the concentration of sodium ion; and the simulation of Warburg factor (σ) was originated from the slope in fitting line of $\omega^{-1/2}$ and Z'.

Galvanostatic intermittent titration technique (GITT) was also used to investigate the Na-storage kinetics of NiS_2@OMGC. During the test, a pulse current of 100 mA/g was applied for 30 min and then rested for 60 min to bring the electrode potentials back to equilibrium (Fig. S11).

During the sodiation and desodiation process, the diffusion coefficient D_{Na+} was calculated using the following equation [22]:

$$D_{Na^+} = \frac{4}{\pi\tau}\left(\frac{m_BV_m}{M_BS}\right)^2\left(\frac{\Delta E_s}{\Delta E_\tau}\right)^2 \tag{7}$$

where m_B is the active mass of the electrode; V_m is the molar volume; M_B is the molar mass of the electrode; S is the electrochemically active area of the electrode; ΔE_s is the difference in open-circuit voltages after two adjacent relaxations;

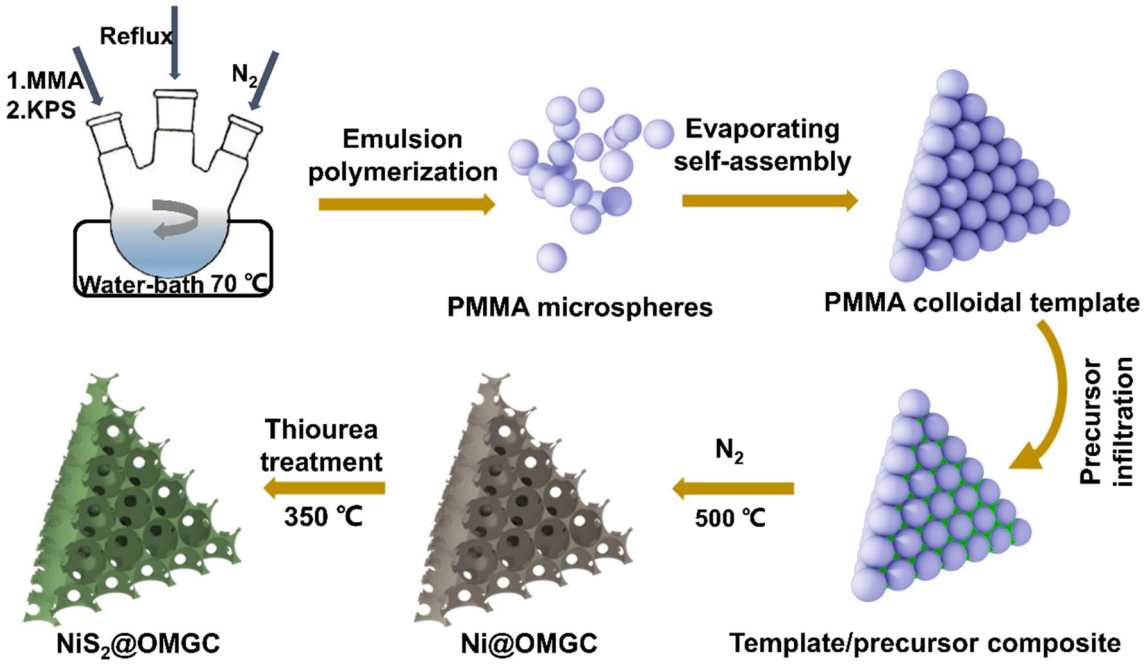

Scheme 1 Schematic illustration of the formation process of NiS_2@OMGC

and ΔE_τ is the voltage difference between the beginning and termination of a single pulse step.

Results and Discussion

Facile Fabrication and Physiochemical Characterizations of NiS_2@OMGC

Scheme 1 depicts the overall synthesizing procedure of the NiS_2@OMGCcomposite. The structurally ordered template of PMMA microspheres (~ 400 nm in diameter, Fig. S1) was first impregnated in a citric acid-chelated nickel nitrate solution, where its void spaces would be filled with Ni salts-formed gel after drying. Followed by nitrogen-protection calcination at 500 °C and a convenient thiourea-treatment process at 350 °C, the precursor could be transformed into the target NiS_2@OMGC composite through a Ni@OMGC intermediate of Ni nanocrystals and GC matrix (Figs. 1 and S2) [23].

Figure 1a, b depicts the SEM images, showing that NiS_2@OMGC inherits the well-defined 3DOM morphology from Ni@OMGC. The TEM images in Fig. 1c, d reveal that the NiS_2 nanoparticles are uniformly embedded in the continuous carbon matrix. Their sizes are distributed within 8.8 ± 1.7 nm (Fig. 1c inset). The high-resolution TEM image (Fig. 1d) further indicates that these NiS_2 nanocrystals are well encapsulated by onion-like GC (up to ~ 10 layers and ~ 0.37 nm in the interlayer spacing, namely d_{002} value). They may expose different crystal faces like (311) (Fig. 1e), (220), (211), (210), and (200), as verified by the diffraction rings-featured selected area electron diffraction (SAED) pattern of NiS_2 phase (JCPDS Card#89-0375; Fig. 1f). Moreover, the elemental mapping (Fig. 1g) demonstrates the uniform distribution of all the elements in the entire 3DOM matrix, including Ni, S, C, and N, identified by EDS at approximately 5.3, 11.4, 82.6, and 0.7 at% (Fig. S3), respectively.

The combined XRD patterns (Fig. 2a) and Raman spectra (Fig. 2b) of NiS_2@OMGC and Ni@OMGC can confirm the composition of the target sample as NiS_2 and GC. By indexing each diffraction peak, it is found that all the cubic Ni phases (JCPDS Card#89-7128) in Ni@OMGC have been converted to cubic NiS_2. As a result of the co-doping of N and S elements during the CH_4N_2S pyrolysis, the d_{002} value of the GC component appears to have increased slightly (from 0.35 to 0.37 nm) [24]. The enhanced Raman *D* band (located at 1347 cm^{-1}, characteristic of disordered carbon) of NiS_2@OMGC and the increased intensity ratio (from 1.76 to 1.98) between the Raman *D* and *G* bands (located at 1589 cm^{-1}, characteristic of sp^2 hybridized GC) both indicate the heteroatom doping. This doping would enhance the material's local conductivity and greatly enrich its defects to accommodate more Na atoms [25]. Figure 2c shows the nitrogen adsorption/desorption isotherms of NiS_2@OMGC. The typical IV-type curve, H3-type hysteresis loop, and sharp N_2 uptake at a relative pressure range of 0.9–1.0 indicate the presence of hierarchical nanopores in this sample,

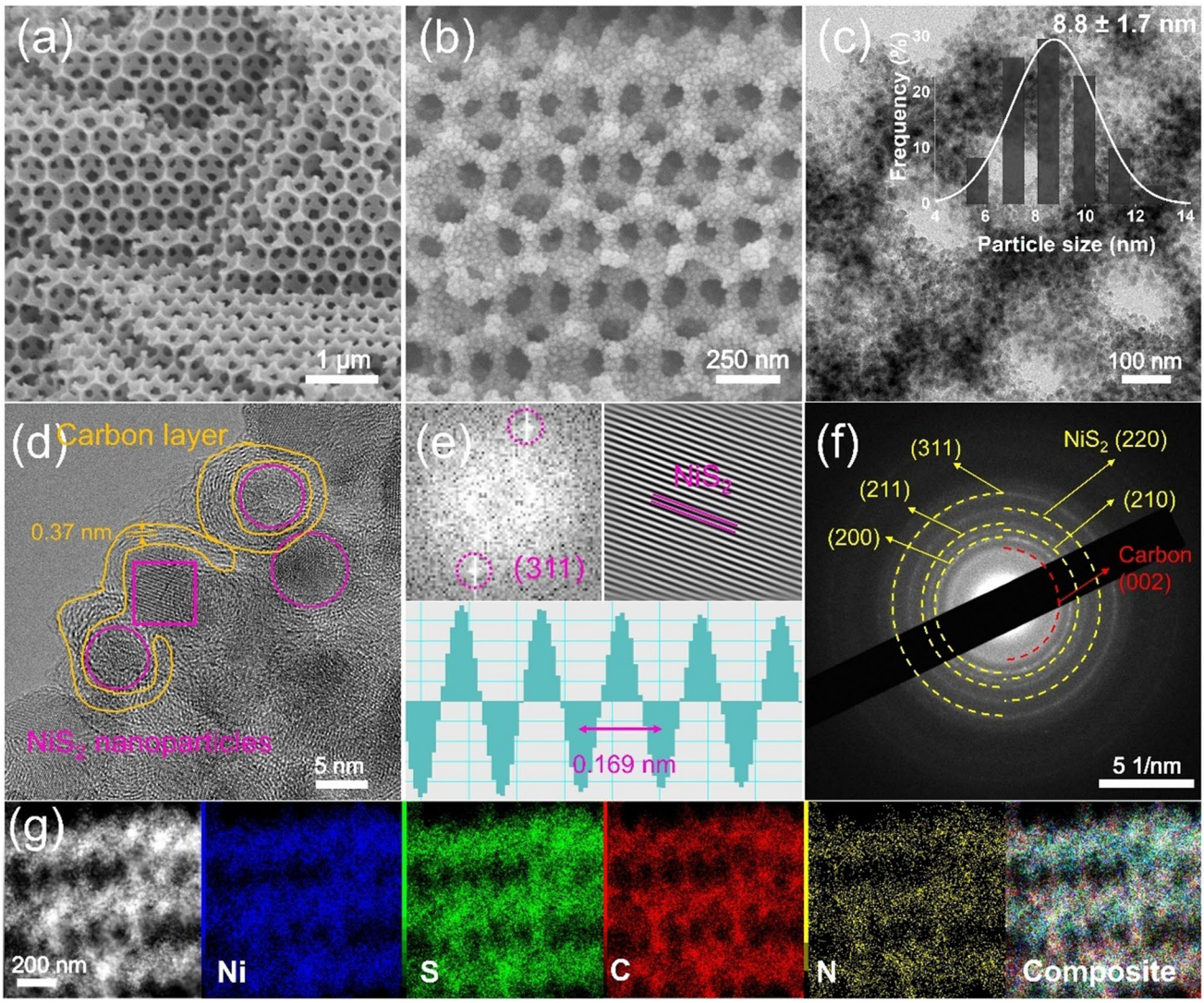

Fig. 1 Architectural feature of NiS_2@OMGC. **a** SEM image of Ni@OMGC. **b** SEM image of NiS_2@OMGC. **c** TEM image together with the size distribution of the encapsulated NiS_2 nanocrystals (inset). **d** HRTEM image of NiS_2@OMGC. **e** Fast Fourier transform image of a single NiS_2 nanocrystal. **f** SAED pattern. **g** Elemental mappings of NiS_2@OMGC

confirmed by the PSD curve based on the adsorption isotherm (Fig. 2c inset). Undoubtedly, such a developed and ordered porous structure would facilitate the mass transfer of both electrolyte and Na^+ ions. This material also demonstrates a relatively large specific surface area, ca. 230.5 m^2/g using the Brunauer–Emmett–Teller method. Although forming the solid electrolyte interface (SEI) made it difficult to achieve a high initial Coulombic efficiency (ICE), it greatly benefits achieving superior ions/charges adsorption required by supercapacitor or pseudocapacitor-type electrodes.

The chemical constituents of NiS_2@OMGC were determined using the analyses of thermogravimetry (TG) in air and XPS. In light of possible reactions ($C\ (s) + O_2\ (g) \rightarrow CO_x\ (g)$ and $NiS_2\ (s) + O_2\ (g) \rightarrow NiO\ (s) + SO_2\ (g)$ [11, 26, 27]) and the staged weight-remaining ratios indicated by the TG curve (Fig. 2d), the contents of NiS_2 and N, S-co-doped GC are estimated to be ca. 68.5 and 31.5 wt%, respectively. Figure 2e–i presents the chemical states of the surface Ni, S, C, N, and O species (ca. 50.2, 6.4, 29.1, 4.7, and 11.4 at%), respectively. The Ni 2*p* spectrum (Fig. 2f) can be deconvoluted into six peaks corresponding to Ni^{2+} (853.4 and 855.6 eV for Ni^{2+} $2p_{3/2}$, 870.9, and 874.0 eV for Ni^{2+} $2p_{1/2}$) and two shakeup satellites, confirming the complete conversion of metallic Ni to NiS_2 [28]. For the S species (Fig. 2g), the two obvious peaks at 161.9 and 162.9 eV (for S $2p_{1/2}$ and $2p_{3/2}$) are correlated with the spin–orbit characteristics of S_2^{2-} in NiS_2. The peak at 164.1 eV is assigned to −C=S− bridging S_2^{2-} and/or −C−S−C− apical S^{2-} ligands [11, 29]. Furthermore, the binding energy at 168.5 eV can be identified

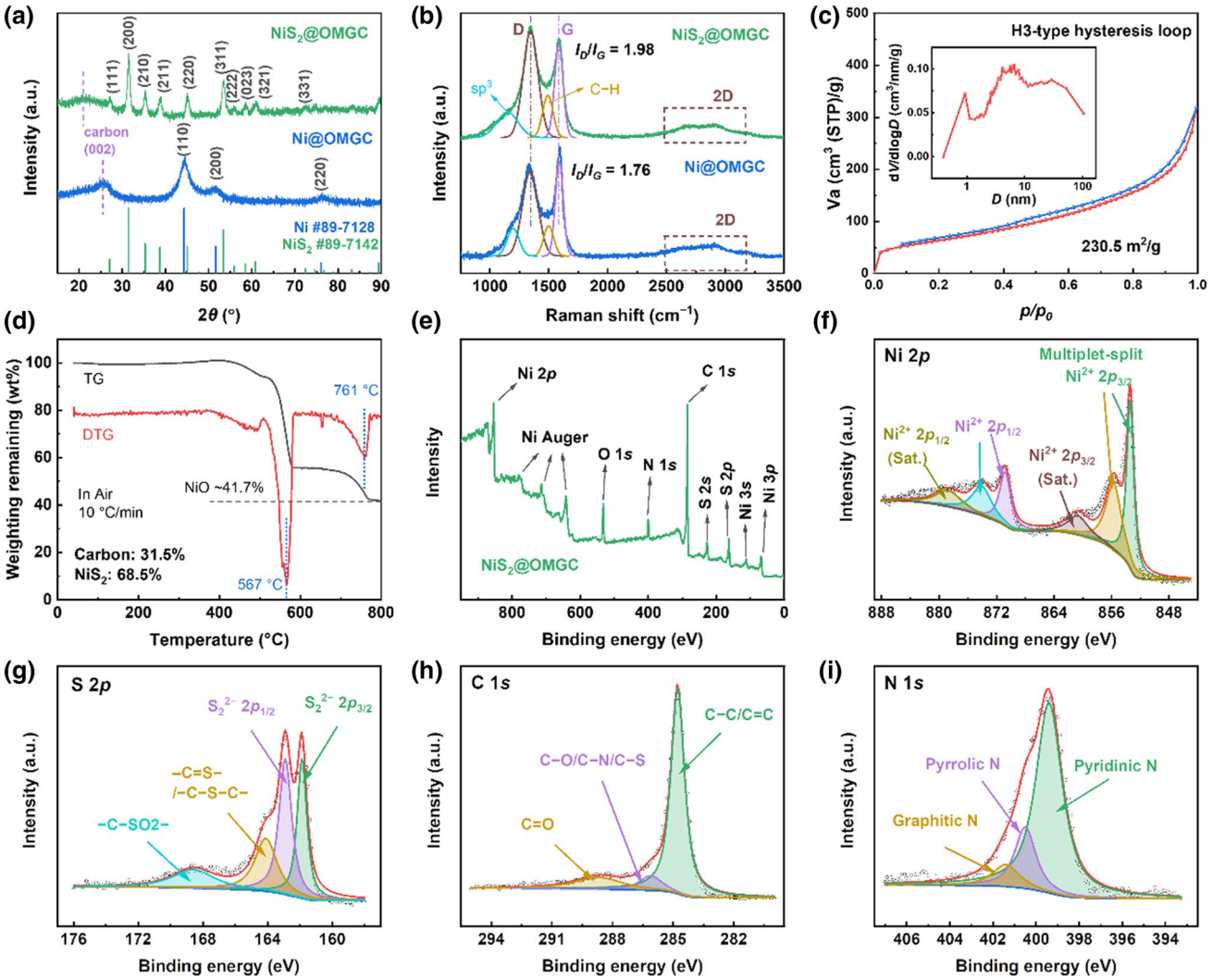

Fig. 2 Microstructure and composition characterizations of NiS_2@OMGC. **a** XRD patterns and **b** Raman spectra of NiS_2@OMGC and Ni@OMGC. **c** Nitrogen adsorption/desorption isotherms and corresponding PSD curve. **d** TG-DTG curves measured in air. **e–i** XPS spectra: **e** full spectrum, **f** Ni 2*p*, **g** S 2*p*, **h** C 1*s*, and **i** N 1*s*

as the $-C-SO_2-$ bond, which is generally related to slight surface oxidation. As to the C 1*s* spectrum (Fig. 2h), the three distinct peaks centered at 284.8, 286.1, and 288.7 eV should indicate that there are mainly three types of carbon species, such as the dominated graphenic C atoms, a few heteroatom-bonded C atoms (e.g., C–O, C–N, and C–S), and some oxidized C atoms on edge (e.g., C=O) [26, 30, 31]. Finally, Fig. 2i depicts the high-resolution XPS spectrum of N 1*s*. It shows that only a tiny fraction of N atoms (8.4 at% by referring to the peak at 401.4 eV) enter the internal network of the GC matrix. The pyridinic N (399.4 eV, 72.7 at%) [22, 23, 30] has a significant proportion for functional defects (or active reaction sites) conducive to local electron conductivity of the composite [32].

Identification of the Electrochemical Na-Storage Performances of NiS_2@OMGC

Figure 3a shows the initial cyclic voltammetry (CV) curves of NiS_2@OMGC measured at a slow scan rate (v) of 0.1 mV/s and between 3.0 and 0.01 V (*vs.* Na^+/Na). SEI was generated during the first cathodic scan as indicated by the intense peak centered at 1.29 V and those distributed between 0.92 and 0.33 V [33], all of which disappeared in the subsequent cycles. After the SEI formation, several pairs of redox peaks are observed over the highly reversible and stable CV curves. The peaks at 1.73/2.06 and 1.54/1.81 V can be attributed to the stepped conversion reaction between NiS_2 and Na_xNiS_2 (i.e., $NiS_2 + xNa^+ + xe^- \leftrightarrow Na_xNiS_2$) [11, 34], whereas the peak of much-enhanced intensity centered

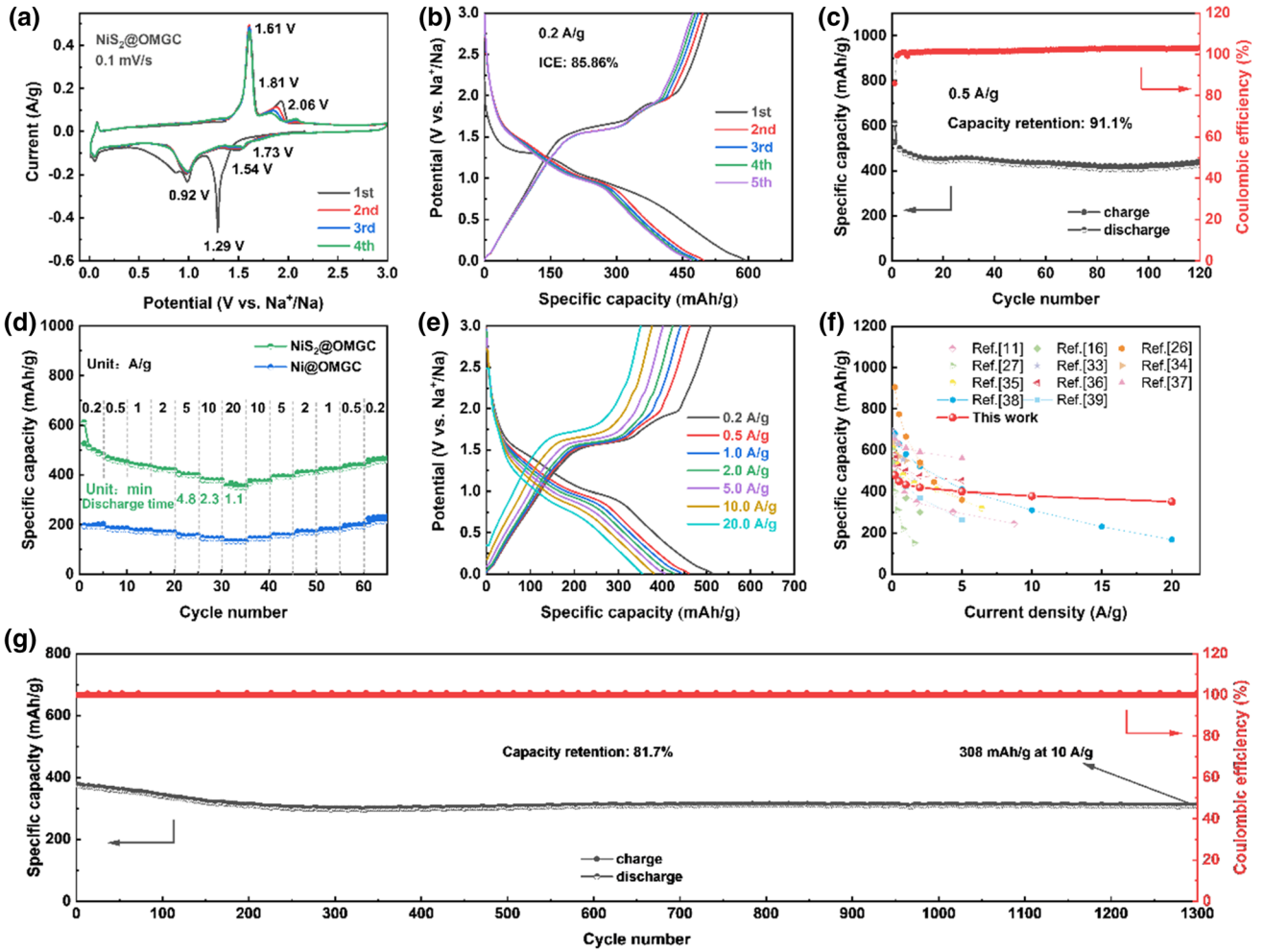

Fig. 3 Electrochemical Na-storage performances of NiS_2@OMGC electrodes. **a** Initial CV curves at 0.1 mV/s. **b** Initial GCD profiles at 0.2 A/g. **c** Cycling performances at 0.5 A/g. **d** Rate performance of Ni@OMGC and NiS_2@OMGC electrodes at 20.0–0.2 A/g. **e** GCD curves at varied current densities from 20.0 to 0.2 A/g. **f** Comparative rate performances of NiS_2@OMGC with other reported NiS_x-based anodes based on discharged capacity. **g** Cycling performances at 10.0 A/g

at 0.92/1.61 V should represent the deeper sodiation and regeneration of the Na_xNiS_2 phase (i.e., $Na_xNiS_2 + (4–x)Na^+ + (4–x)e^- \leftrightarrow Ni + 2Na_2S$) [11, 34]. The sodiation/desodiation voltages from its initial galvanostatic charge/discharge (GCD) profiles at 0.2 A/g are in good agreement with the CV curves (Fig. 3b). Moreover, the NiS_2@OMGC electrode delivers a discharge and charge capacities of 597.9 and 513.4 mAh/g, respectively, achieving a desirable ICE of 85.86%. Subsequently, after 120 cycles at 0.5 A/g, a high reversible capacity of 439.4 mAh/g is retained, with high-level capacity retention (ca. 91.2%) relative to that of the sixth cycle (Figs. 3c and S4). More importantly, the rate performance of Ni@OMGC and NiS_2@OMGC electrodes over a wide range of current densities is shown in Fig. 3d; their GCD curves at different current densities are presented in Figs. S5 and 3e. Typically, the initially reversible capacities of NiS_2@OMGC electrodes were measured to be ~513.4, 468.8, 437.3, 421.3, 400.3, 378.0, and 355.7 mAh/g at 0.2, 0.5, 1.0, 2.0, 5.0, 10.0, and 20.0 A/g, respectively. When the current density was gradually reduced to 0.2 A/g (Fig. 3d), a reversible capacity of ca. 457.0 mAh/g and high capacity retention (ca. 89.0%) were obtained. Meanwhile, Ni@OMGC electrodes have a relatively lower specific capacity. Nevertheless, the Ni@OMGC electrodes exhibit a highly stable capacity even if the current increases 100 times. Conversely, the NiS_2@OMGC electrode's performance is synergistically determined by its NiS_2 phase with high theoretical specific capacity and extremely stable OMGC matrix. Compared with many other NiS_x-based electrodes for SIBs [11, 16, 26, 27, 33–39], such rate performance gives NiS_2@OMGC a significant competitive advantage, especially at high current densities (Fig. 3f). However, the large-pore structure would inevitably compromise the volumetric performances of NiS_2@OMGC. Nevertheless, it still

outperforms many other electrodes of the same kind for SIBs as well as its precursor (nearly four times that of the initial Ni@OMGC; refer to Fig. 3d) due to its two superior compositions with relatively larger specific capacities (Fig. S6). All of these illustrate the excellent electrochemical energy storage (EES) advantages of NiS_2@OMGC, especially in applications that do not require high volumetric performance, such as grid-scale battery energy storage stations. We further checked its long-term cycling performances at 10.0 A/g (Fig. 3g). An inevitable capacity loss occurred in the initial tens of cycles before highly stable cycling, which may be related to the slow dissolution and loss of a small amount of S elements [40]. Typically, the reversible capacities reached 308.4 mAh/g after running 1300 cycles at 10.0 A/g. Such a good rate performance and cycling stability, originating from the highly stable structure (Fig. S7), can fully demonstrate the rational composition and structural design of the NiS_2@OMGC composite.

Electrochemical Na-Storage Mechanism and Kinetic Analyses of NiS_2@OMGC

Charge storage in an electrode material is achieved either by surface-controlled ion adsorption (like supercapacitors) or solid-state ion diffusion (like batteries). Therefore, it is feasible to distinguish ion behavior in CV measurements by monitoring the response current (i) in an electrochemical reaction as described by the power-law equation: $i = av^b$, where a and b are constants when plotting $\log(v)$ *vs.* $\log(i)$ [41]. For fast capacitive ion storage, the b value, namely the slope of the fitted linear plots of $\log(v)$ with respect to $\log(i)$, is close to 1. However, a typical diffusion-controlled battery behavior has a value of 0.5. Hence, a series of CV measurements were performed between 3.0 and 0.01 V (*vs.* Na^+/Na) by varying scan rates from 2.0 to 0.1 mV/s to explain the high-rate Na-storage performance of NiS_2@OMGC. The estimated b values for the typical seven-set CV redox peaks labeled in Fig. 4a are all above 0.78 and even reach 0.92−0.99 for the three anodic ones, as shown in Fig. 4a, b. Thus, the sodiation and desodiation of the NiS_2@OMGC electrode (or its two components) are both highly desirable (pseudo-)capacitive behaviors. To support this statement, the capacitive contributions at different scan rates were calculated using the approximate equation $i(v) = k_1v + k_2v^{0.5}$, where $i(v)$ and the two k values represent the total response current at a specific voltage (V) and the fitting constants, respectively [42]. The charge storage in the NiS_2@OMGC electrode is almost dominated by the (pseudo-)capacitive behavior, as shown by the nearly overlapping CV curves (Figs. 4c and S8). The capacitive contribution reaches ~100% at small scan rates (Fig. 4d), accounting for its excellent Na-storage rate performance and cycling stability. Many factors about ion and electron conduction properties ($Na^+ + e^- \rightleftharpoons Na^0$) can be used to interpret the extraordinarily "extrinsic" pseudocapacitive EES performances of NiS_2@OMGC, such as its well-defined 3DOM morphology with both developed nanoporous structure and excellent overall electrical conductivity, its heteroatom-doped GC matrix with both superior interlayer spacing and local electrical conductivity, and its monodispersed NiS_2 active constitutes with all dimensions less than 10 nm [43].

To further investigate the NiS_2@OMGC electrodes, in situ EIS [44] and GITT [21] techniques were used for Na-storage kinetics. Figure 4e, f depicts the typical Nyquist plots of a mature NiS_2@OMGC-based electrode upon the repeated potential drop and increase. The Randle-type equivalent circuit can fit all plots well (Fig. S9), showing that the potential gradually decreased from 3.0 to 0.01 V (corresponding to the sodiation process). And the total resistance (R_{tot}) is composed of the intrinsic resistances from the electrode, electrolyte, and separator (R_s), the interfacial resistance related to the SEI (R_{sei}), and the charge transfer resistance at the electrode–SEI interface (R_{ct}) (Fig. S10) [45], only increases by 4.6 $\Omega \cdot cm^2$ (from 15.9 to 20.5 $\Omega \cdot cm^2$; Fig. 4g). Moreover, two large and one slight stepwise increase seems to appear around 1.6/0.9 V and 0.3 V, respectively, in good line with the electrochemical reaction potentials over the CV curves. During the desodiation process, similar phenomena occur, but the phase transformation of metallic Ni to nonconductive NiS_2 leads to a large R_{tot} increase (by 5.0 $\Omega \cdot cm^2$) between 1.6 and 2.1 V. Figure 4e, f depicts the regular evolutions of the Warburg regions, namely the linear part of the Nyquist plots associated with the Na^+ ion diffusion in the electrode. Thus, the apparent diffusion coefficients of Na^+ ions (D_{Na+}) at various stages can be obtained, shown in Fig. 4g, based on the reported Warburg impedance method (in the supporting information) [44]. It is found that the D_{Na+} values range between 10^{-9} and 10^{-8} cm^2/s, ca. 8.3×10^{-10} cm^2/s for the NiS_2-based conversion reaction and 7.4×10^{-9} cm^2/s for the GC-based intercalation reaction. Besides, the Ni-NiS_2 redox reactions (such as at the discharged 1.6 and 1.1 V, as well as the charged 1.6 and 2.0 V) would promote the Na^+ ion diffusion, which may result from the improved ion transfer kinetics at their constantly reconstructed interfaces. Consistent conclusions could be drawn from the GITT experiment (Figs. 4h and S11), including the order of magnitude of the D_{Na+} values and their variation tendency [21]. Overall, the different Na^+ diffusion rates of its two components for this specific NiS_2@OMGC electrode indicate that the multilayered GC shell would provide Na^+ ions with a convenient diffusion pathway to approach the encapsulated NiS_2 nanocrystal rather than impede this process. The relatively small three dimensions of the NiS_2 nanocrystals over the entire conductive graphenic matrix allow this phase to undergo rapid surface redox reactions, ensuring the superior

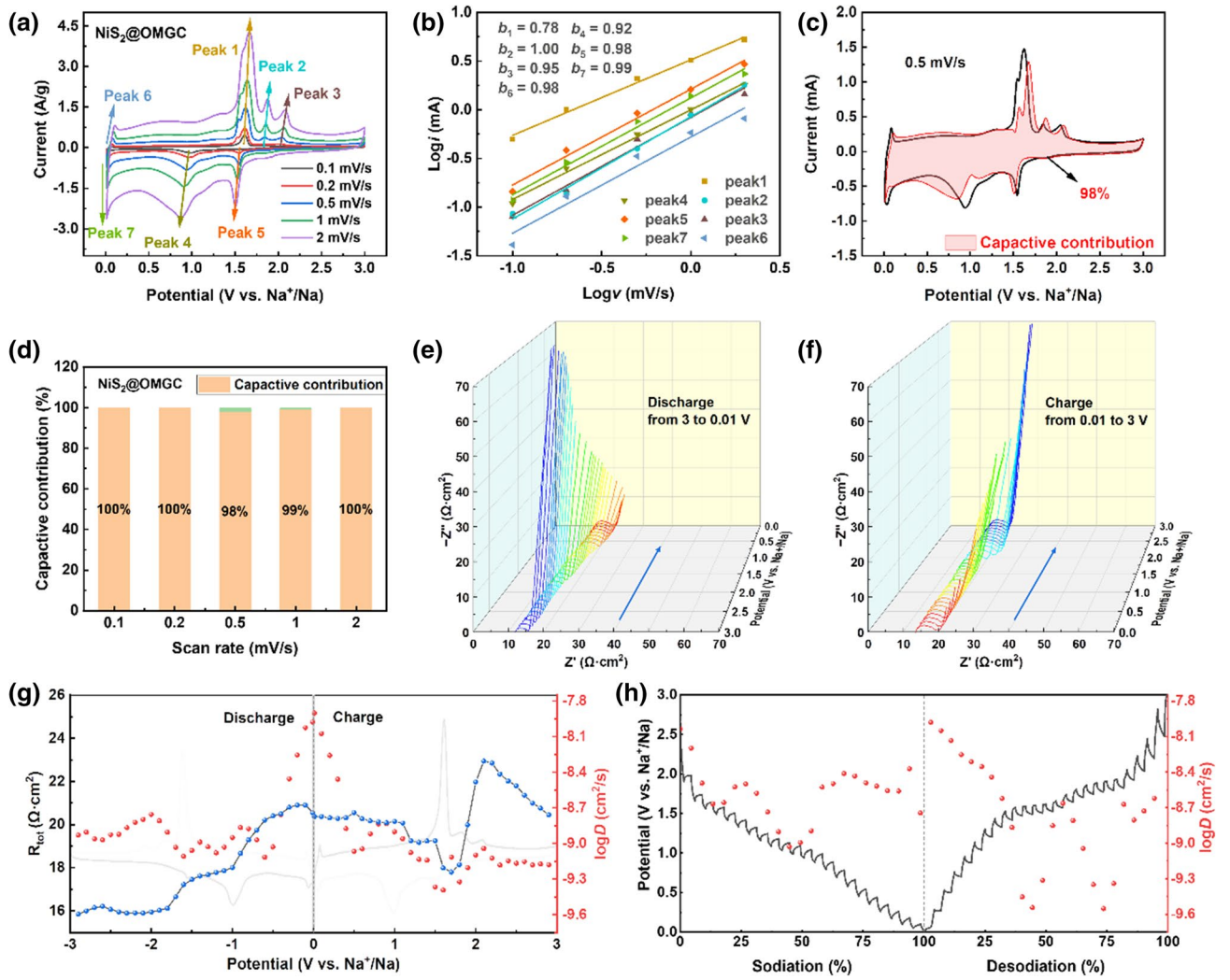

Fig. 4 Identification of the electrochemical Na-storage mechanism of NiS_2@OMGC. **a** CV curves at scan rates varied from 2 to 0.1 mV/s. **b** Plots of log(*i*) *vs.* log(*ν*) of the cathodic/anodic peaks marked in (**a**). **c** Capacitive contribution (shaded area) to the total charge storage at 0.5 mV/s. **d** Capacitive contribution ratios at each of the CV scan rates. **e** In situ Nyquist plots with stepped potential drop and **f** in situ Nyquist plots with stepped potential increase between 3.0 and 0.01 V. **g** Evolutions of the R_{tot} (blue points) and D_{Na+} (red points) values calculated by the EIS methods. **h** Evolution of the D_{Na+} values (red points) calculated from the GITT profile (black line) of NiS_2@OMGC

"extrinsic" pseudocapacitive performance of NiS_2@OMGC throughout the EES process [43, 46].

Performance Evaluation of a NiS_2@OMGC-based SIHC Device

In order to further evaluate the potential of NiS_2@OMGC in practical application, SIHC full-cell devices were fabricated using AC as cathode and 0.8 mol/L $NaPF_6$ dissolved in DEGDME as electrolyte (denoted as NiS_2@OMGC//AC SIHC, with the mass ratio of NiS_2@OMGC and AC at 1:3). During discharging (shown in Fig. 5a), when cations (i.e., DEGDME-Na^+) are stored in NiS_2@OMGC, anions from the electrolyte (PF_6^-) are absorbed by AC. Consequently, a wide voltage window of 4.0–0.01 V was applied to operate the SIHC device because of the safety voltages of the as-applied electrolyte and electrodes (i.e., 4.0–2.5 V and 3.0–0.01 V for AC and NiS_2@OMGC, respectively; Figs. 5b and S12). Figure 5c depicts its typical CV curves at scan rates ranging from 0.5 to 5 mV/s, where the approximate rectangular shape indicates the superior reversibility and remarkably pseudocapacitive feature of this device [21, 46]. Figure S13 depicts specific capacitances of the device, showing that the capacitance reaches up to 43.1 F/g at 1 mV/s. The approximately linear profile of GCD curves at 20.0–0.1 A/g, together with their symmetric triangular shape, also demonstrates the nearly ideal capacitive behavior of the NiS_2@OMGC//AC SIHC device (Fig. 5d, e). In particular,

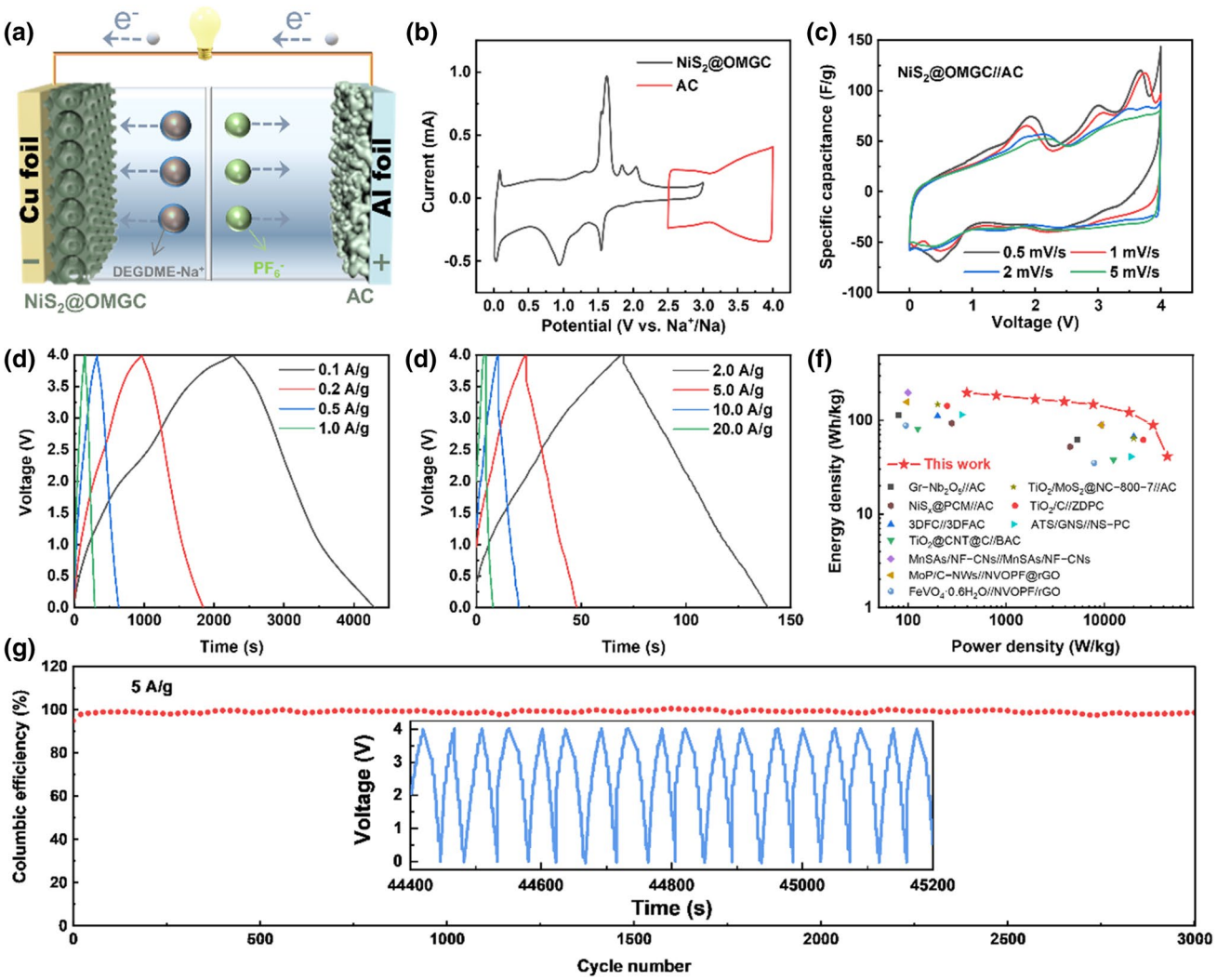

Fig. 5 Electrochemical performances of the NiS_2@OMGC//AC SIHC device. **a** Schematic illustration of the working mechanism of the device. **b** Individual CV curves of its two electrodes in a Na half-cell. **c** CV curves at different scan rates ranged from 5 to 0.5 mV/s. GCD profiles at current densities of **d** 1.0–0.1 A/g and **e** 20.0–2.0 A/g. **f** Compared Ragone plots of the NiS_2@OMGC//AC SIHC device with other reported similar systems. **g** Cycling performance at 5.0 A/g

its specific capacitances were calculated to be 30.8, 32.5, 33.9, 35.7, 37.3, 38.9, 42.1, and 44.7 F/g at 20.0, 10.0, 5.0, 2.0, 1.0, 0.5, 0.2 and 0.1 A/g (Fig. S14), respectively, rather competitive compared with the reported values (Table S1). The results agreed with the CV results and indicated its superior rate capability. A Ragone plot of power density *vs.* energy density (based on the total active mass) was also obtained to demonstrate the SIHC device. As shown in Fig. 5f, the maximum energy density of 197.4 Wh/kg was achieved at 0.1 A/g, following a power density of 398.8 W/kg and thus a current-drain time (*E*/*P*) of 29.7 min. The maximum power density of 43.9 kW/kg was achieved at 20.0 A/g, following an energy density of 41.3 Wh/kg and a current-drain time of 3.4 s. Such a comprehensive performance is far superior compared with most of those reported SIHCs [21, 30, 32, 38, 42, 47–51]. Finally, we examined its long-term cycling stability at a large current density of 5.0 A/g. Figure 5g exhibits nearly 100% of Coulombic efficiency over all 3000 cycles, confirming the structural stability of NiS_2@OMGC as a high-capacity anode for SIHC.

Conclusion

We developed a NiS_2@OMGC composite with numerous ultrasmall NiS_2 nanocrystals embedded in a 3DOM-structured N, S co-doped GC matrix using a facile thiourea pyrolysis-assisted colloidal crystal template method. The NiS_2@OMGC electrode, which benefits from the distinguished 3DOM nano–microstructure, ultrafine NiS_2 nanoparticles,

and GC matrix, demonstrates a dominant pseudocapacitive energy storage mechanism and excellent Na-storage performances, such as ultrahigh-rate capabilities and long-term cycling stability to endow a SIHC with simultaneously large energy and power densities. Our developed strategy could be applied to other metal sulfides/oxides/phosphides/selenide-based electrodes for various EES devices.

Supplementary Information The online version contains supplementary material available at https://doi.org/10.1007/s12209-022-00338-7.

Acknowledgements This work is supported by the National Natural Science Foundation of Tianjin (No. 20JCQNJC01280) and the National Natural Science Foundation of China (No. 21905201). The authors acknowledge the support of the scientific research project from China Three Gorges Corporation (No. 202103406). The corresponding author was supported by Tohoku University and JSPS KAKENHI (No. JP16J06828).

Declarations

Conflict of interest The authors declare that they have no conflict of interest.

Open Access This article is licensed under a Creative Commons Attribution 4.0 International License, which permits use, sharing, adaptation, distribution and reproduction in any medium or format, as long as you give appropriate credit to the original author(s) and the source, provide a link to the Creative Commons licence, and indicate if changes were made. The images or other third party material in this article are included in the article's Creative Commons licence, unless indicated otherwise in a credit line to the material. If material is not included in the article's Creative Commons licence and your intended use is not permitted by statutory regulation or exceeds the permitted use, you will need to obtain permission directly from the copyright holder. To view a copy of this licence, visit http://creativecommons.org/licenses/by/4.0/.

References

1. Zuo W, Li R, Zhou C et al (2017) Battery-supercapacitor hybrid devices: recent progress and future prospects. Adv Sci 4(7):1600539
2. Wang H, Zhu C, Chao D et al (2017) Nonaqueous hybrid lithium-ion and sodium-ion capacitors. Adv Mater 29(46):1702093
3. Deng X, Zou K, Cai P et al (2020) Advanced battery-type anode materials for high-performance sodium-ion capacitors. Small Methods 4(10):2000401
4. Ding J, Hu W, Paek E et al (2018) Review of hybrid ion capacitors: from aqueous to lithium to sodium. Chem Rev 118(14):6457–6498
5. Yuan Y, Wang CC, Lei KX et al (2018) Sodium-Ion hybrid capacitor of high power and energy density. ACS Cent Sci 4(9):1261–1265
6. Cai P, Zou K, Deng X et al (2021) Comprehensive understanding of sodium-ion capacitors: definition, mechanisms, configurations, materials, key technologies, and future developments. Adv Energy Mater 11(16):2003804
7. Tan X, Mo R, Xu J et al (2022) High performance sodium ion anodes based on Sn_4P_3 encapsulated within amphiphilic graphene tubes. Adv Energy Mater 12(2):2102345
8. Hwang JY, Myung ST, Sun YK (2017) Sodium-ion batteries: present and future. Chem Soc Rev 46(12):3529–3614
9. Yabuuchi N, Kubota K, Dahbi M et al (2014) Research development on sodium-ion batteries. Chem Rev 114(23):11636–11682
10. Xiao Y, Lee SH, Sun YK (2017) The application of metal sulfides in sodium ion batteries. Adv Energy Mater 7(3):1601329
11. Zhao G, Zhang Y, Yang L et al (2018) Nickel chelate derived NiS_2 decorated with bifunctional carbon: an efficient strategy to promote sodium storage performance. Adv Funct Mater 28(41):1803690
12. Vu TT, Park S, Park J et al (2020) Investigation of superior sodium storage and reversible Na_2S conversion reactions in a porous NiS_2@C composite using in operando X-ray diffraction. J Mater Chem A 8(46):24401–24407
13. Hu M, Ju Z, Bai Z et al (2019) Revealing the critical factor in metal sulfide anode performance in sodium-ion batteries: an investigation of polysulfide shuttling issues. Small Methods 4(1):1900673
14. Yan Z, Xiao J, Lai W et al (2019) Nickel sulfide nanocrystals on nitrogen-doped porous carbon nanotubes with high-efficiency electrocatalysis for room-temperature sodium-sulfur batteries. Nat Commun 10(1):4793
15. He H, Chen C, Chen Z et al (2020) Ni_3S_2@S-carbon nanotubes synthesized using NiS_2 as sulfur source and precursor for high performance sodium-ion half/full cells. Sci China Mater 63(2):216–228
16. Chen Q, Sun S, Zhai T et al (2018) Yolk-shell NiS_2 nanoparticle-embedded carbon fibers for flexible fiber-shaped sodium battery. Adv Energy Mater 8(19):1800054
17. Xu YG, Liu J, Kong LB (2021) Reduced graphene oxide decorated amorphous NiS_2 nanosheets as high-performance anode materials for enhanced sodium-ion hybrid capacitors. Ionics (Kiel) 27(8):3315–3325
18. Li W, Huang B, Liu Z et al (2021) NiS_2 wrapped into graphene with strong Ni–O interaction for advanced sodium and potassium ion batteries. Electrochim Acta 369:137704
19. Liu ZC, Yuan XH, Zhang SS et al (2019) Three-dimensional ordered porous electrode materials for electrochemical energy storage. NPG Asia Mater 11:12
20. Li H, Zhang L, Dai H et al (2009) Facile synthesis and unique physicochemical properties of three-dimensionally ordered macroporous magnesium oxide, gamma-alumina, and ceria−zirconia solid solutions with crystalline mesoporous walls. Inorg Chem 48(10):4421–4434
21. Hu X, Wang GX, Li JW et al (2021) Significant contribution of single atomic Mn implanted in carbon nanosheets to high-performance sodium-ion hybrid capacitors. Energy Environ Sci 14(8):4564–4573
22. Shen Y, Jiang Y, Yang Z et al (2022) Electronic structure modulation in MoO_2 /MoP heterostructure to induce fast electronic/ionic diffusion kinetics for lithium storage. Adv Sci 9(6):2104504
23. Ji K, Han J, Wang B et al (2018) Nanocrystalline C–Ni hybrid nanoporous monoliths for large-capacity and ultrahigh-rate energy storage. https://doi.org/10.2139/ssrn.3207211
24. Jin Q, Wang K, Feng P et al (2020) Surface-dominated storage of heteroatoms-doping hard carbon for sodium-ion batteries. Energy Stor Mater 27:43–50
25. Li XY, Han ZY, Yang WH et al (2021) 3D ordered porous hybrid of ZnSe/N-doped carbon with anomalously high Na^+ mobility and ultrathin solid electrolyte interphase for sodium-ion batteries. Adv Funct Mater 31(50):2106194
26. Yang L, Hong W, Zhang Y et al (2019) Hierarchical NiS_2 modified with bifunctional carbon for enhanced potassium-ion storage. Adv Funct Mater 29(50):1903454

27. Bi R, Zeng C, Huang H et al (2018) Metal–organic frameworks derived hollow NiS_2 spheres encased in graphene layers for enhanced sodium-ion storage. J Mater Chem A 6(29):14077–14082
28. Liang S, Shi H, Yu Z et al (2021) Uncovering the design principle of conversion-based anode for potassium ion batteries via dimension engineering. Energy Stor Mater 34:536–544
29. Ito Y, Cong W, Fujita T et al (2015) High catalytic activity of nitrogen and sulfur co-doped nanoporous graphene in the hydrogen evolution reaction. Angew Chem Int Ed 54(7):2131–2138
30. Jiang Y, Shen Y, Dong J et al (2019) Surface pseudocapacitive mechanism of molybdenum phosphide for high-energy and high-power sodium-ion capacitors. Adv Energy Mater 9(27):1900967
31. Yan R, Leus K, Hofmann JP et al (2020) Porous nitrogen-doped carbon/carbon nanocomposite electrodes enable sodium ion capacitors with high capacity and rate capability. Nano Energy 67:104240
32. Li YZ, Wang HW, Wang LB et al (2019) Ultrafast Na^+-storage in TiO_2-coated MoS_2@N-doped carbon for high-energy sodium-ion hybrid capacitors. Energy Stor Mater 23:95–104
33. Wu J, Liu S, Rehman Y et al (2021) Phase engineering of nickel sulfides to boost sodium- and potassium-ion storage performance. Adv Funct Mater 31(27):2010832
34. Lin Y, Qiu Z, Li D et al (2018) NiS_2@CoS_2 nanocrystals encapsulated in N-doped carbon nanocubes for high performance lithium/sodium ion batteries. Energy Stor Mater 11:67–74
35. Zhao W, Ci S, Hu X et al (2019) Highly dispersed ultrasmall NiS_2 nanoparticles in porous carbon nanofiber anodes for sodium ion batteries. Nanoscale 11(11):4688–4695
36. Guan S, Wang T, Fu X et al (2020) Coherent SnS_2/NiS_2 heteronanosheet arrays with fast charge transfer for enhanced sodium-ion storage. Appl Surf Sci 508:145241
37. Shuang W, Huang H, Kong L et al (2019) Nitrogen-doped carbon shell-confined Ni_3S_2 composite nanosheets derived from Ni-MOF for high performance sodium-ion battery anodes. Nano Energy 62:154–163
38. Li S, He W, Liu B et al (2020) One-step construction of three-dimensional nickel sulfide-embedded carbon matrix for sodium-ion batteries and hybrid capacitors. Energy Stor Mater 25:636–643
39. Zou Z, Wang Q, Yan J et al (2021) Versatile interfacial self-assembly of $Ti_3C_2T_x$ MXene based composites with enhanced kinetics for superior lithium and sodium storage. ACS Nano 15(7):12140–12150
40. Wang F, Han F, He Y et al (2021) Unraveling the voltage failure mechanism in metal sulfide anodes for sodium storage and improving their long cycle life by sulfur-doped carbon protection. Adv Funct Mater 31(3):2007266
41. Wang J, Polleux J, Lim J et al (2007) Pseudocapacitive contributions to electrochemical energy storage in TiO_2 (anatase) nanoparticles. J Phys Chem C 111(40):14925–14931
42. Li H, Lang J, Lei S et al (2018) A high-performance sodium-ion hybrid capacitor constructed by metal-organic framework-derived anode and cathode materials. Adv Funct Mater 28(30):1800757
43. Simon P, Gogotsi Y, Dunn B (2014) Materials science. Where do batteries end and supercapacitors begin? Science 343(6176):1210–1211
44. Ji K, Han J, Hirata A et al (2019) Lithium intercalation into bilayer graphene. Nat Commun 10(1):275
45. Gaberscek M (2021) Understanding Li-based battery materials via electrochemical impedance spectroscopy. Nat Commun 12(1):6513
46. Ghidiu M, Lukatskaya MR, Zhao MQ et al (2014) Conductive two-dimensional titanium carbide "clay" with high volumetric capacitance. Nature 516(7529):78–81
47. Yang B, Chen J, Lei S et al (2018) Spontaneous growth of 3D framework carbon from sodium citrate for high energy- and power-density and long-life sodium-ion hybrid capacitors. Adv Energy Mater 8(10):1702409
48. Zhu YE, Yang L, Sheng J et al (2017) Fast sodium storage in TiO_2@CNT@C nanorods for high-performance Na-ion capacitors. Adv Energy Mater 7(22):1701222
49. Wang X, Li Q, Zhang L et al (2018) Caging Nb_2O_5 nanowires in PECVD-derived graphene capsules toward bendable sodium-ion hybrid supercapacitors. Adv Mater 30(26):1800963
50. Sun ZQ, Zhu KJ, Liu P et al (2021) Rapid kinetics of Na-ion storage in bimetallic sulfide composite. Energy Stor Mater 41:32–40
51. Dong J, He Y, Jiang Y et al (2020) Intercalation pseudocapacitance of $FeVO_4{\cdot}nH_2O$ nanowires anode for high-energy and high-power sodium-ion capacitor. Nano Energy 73:104838

Dr. Kemeng Ji completed his doctorate in Materials Science at Tohoku University (Japan, 2018) and in Applied Chemistry at Beijing University of Technology (China, 2014), respectively. He worked in Tohoku University as a fellow of Japan Society for the Promotion of Scie nce (JSPS) from 2016 to 2018, and in University of Tsukuba as a visiting researcher from 2017 to 2018. In 2019, he joined the faculty of Tianjin University as an associate professor by Peiyang Scholars Program, and now works at School of Chemical Engineering and Technology. His research interests focuses on the design and development of nanoporous functional materials for energy storage and catalysis related applications.